Research Square

Preprints are preliminary reports that have not undergone peer review.
They should not be considered conclusive, used to inform clinical practice,
or referenced by the media as validated information.

From physical hazard to integrated risk: Dynamic snowmelt flood risk across the Tibetan Plateau

Chuhan Kong
Chinese Academy of Sciences
Min Xu
xumin@lzb.ac.cn
Chinese Academy of Sciences

Article

Keywords: Tibetan Plateau, Snowmelt flood, Flood risk assessment, Risk dynamics, Hazard–risk divergence

Posted Date: November 26th, 2026

DOI: https://doi.org/10.21203/rs.3.rs-11801937/v1

License: This work is licensed under a Creative Commons Attribution 4.0 International License.
Read Full License

Additional Declarations: No competing interests reported.

From physical hazard to integrated risk: Dynamic snowmelt flood risk across the Tibetan Plateau

Chuhan Kong [1,2], Min Xu [1*]

[1] *State Key Laboratory of Cryospheric Science and Frozen Soil Engineering, Northwest Institute of Eco-Environment and Resources, Chinese Academy of Sciences, Lanzhou, 730000, China*

[2] *School of Mathematics and Physics, Lanzhou Jiaotong University, Lanzhou 730070, China*

** Corresponding author. E-mail addresses: xumin@lzb.ac.cn (Min Xu)*

ABSTRACT

Snowmelt flood poses an increasingly severe challenge to the Tibetan Plateau; however, due to a lack of adequate integration between physical and socioeconomic dimensions, the regional risks associated with them remain poorly understood. This study developed a comprehensive evaluation framework that integrates hazard, exposure, and vulnerability to assess the risks of snowmelt flood on the Tibetan Plateau. Based on GLDAS data from 1980 to 2025, this study analyzes changes in peak flood intensity and occurrence timing and evaluates the comprehensive risks for the three periods during 1991-2000, 2001-2010, and 2011-2020. Through combined weighting, CatBoost–SHAP, and univariate sensitivity analysis, the study identifies the relative importance of indicators and tests the robustness of the evaluation. The results indicate that snowmelt flood characteristics exhibit significant spatiotemporal heterogeneity, and there is a clear divergence between physical

hazard and comprehensive risk. In 2000, 2010, and 2020, the proportions of high-risk and extremely high-risk areas were 36.6%, 39.1%, and 22.7%, respectively, while the proportions of high-vulnerability and extremely high-vulnerability areas decreased from 43.5% to 19.3%. The SHAP analysis revealed significant differences in the contributions of 11 key watershed indicators, with sensitivity indicators related to the rural agricultural workforce standing out in most watersheds. Under moderate weight perturbations, risk classification maintained a high degree of consistency. The study emphasizes the importance of integrating natural and socioeconomic dimensions and provides a basis for sub-watershed-level snowmelt flood risk management and climate adaptation.

Key words: Tibetan Plateau; Snowmelt flood; Flood risk assessment; Risk dynamics; Hazard–risk divergence

1. Introduction

Climate change is reshaping hydrological processes in alpine regions by altering snow accumulation, snowmelt processes, and the seasonality of runoff. These changes affect the timing and magnitude of snowmelt flood, but there are significant regional differences in responses to climate warming[1,2]. In addition to changes in hydrological characteristics, snowmelt flood may also

threaten ecosystems, infrastructure, and human livelihoods, particularly in high-altitude regions where human activities are closely linked to climate-sensitive water resources[3]. However, focusing solely on changes in the physical hazards of flooding may not fully reflect the broader impacts of snowmelt flood, highlighting the need to understand these risks from a perspective that integrates natural and human systems.

The Tibetan Plateau, commonly referred to as the “Third Pole,” is highly sensitive to climate change, and its complex cryosphere and hydrological processes give rise to a variety of mountain hazards[4,5]. Previous studies have examined the flood formation processes in the plateau region and their hydrometeorological controlling factors[6], while recent research has further quantified the contribution of snowmelt to peak discharge in a single watershed[7]. In addition to natural physical processes, existing studies have also assessed the comprehensive risk of snow-related disasters, various meteorological hazards, and the exposure and vulnerability of socioeconomic systems[5,8,9]. However, these studies have primarily focused on a single hazard type, specific watersheds, or specific groups of affected populations, and there remains an insufficient understanding of the spatiotemporal evolution of the comprehensive risk of snowmelt flood. In particular, it remains unclear how physical hazards interact with human exposure and vulnerability in different regions, and how the relative contributions of risk indicators vary over time and across watersheds.

Furthermore, the impact of indicator weighting methods on the spatial patterns of comprehensive risk, as well as their sensitivity, requires further assessment. Addressing these issues is crucial for moving beyond hazard-centered assessment models and gaining a comprehensive understanding of snowmelt flood risks on the Tibetan Plateau.

To address the aforementioned research gaps, this study developed a comprehensive analytical framework to investigate the spatiotemporal evolution of snowmelt flood risks in the Chinese Tibetan Plateau region. First, using GLDAS snowmelt runoff data from 1980 to 2025, we analyzed the characteristics of changes in the annual maximum magnitude and timing of snowmelt flood. Second, we established a comprehensive hazard–exposure–vulnerability assessment framework and, by combining objective and subjective weighting methods, evaluated the comprehensive risk for the three time periods of 2000, 2010, and 2020. Third, by combining the CatBoost and SHAP methods, we identified the relative contributions and spatial heterogeneity of key risk indicators across 11 major river basins. We also conducted a sensitivity analysis using single-factor perturbation to assess the impact of changes in indicator weights on the robustness of the risk assessment results. By linking hydrological changes in the cryosphere to spatially heterogeneous socioeconomic conditions, this study reveals the differences between physical hazard and comprehensive risk, providing a scientific basis for formulating more

84 targeted climate adaptation and disaster risk management strategies in alpine
85 regions.

86 2. Study area

87 The Chinese part of the Tibetan Plateau (CTP) is one of the world's highest
88 and largest plateau regions (Fig. 1), with a total area of approximately
89 $2.58 \times 10^6\ km^2$ and an average elevation of about 4,400 m. It encompasses
90 the Tibet Autonomous Region, Qinghai Province, and parts of Xinjiang, Gansu,
91 Sichuan, and Yunnan. As the source of several major Asian rivers, the Tibetan
92 Plateau plays a crucial role in water conservation and hydrological regulation[10].
93 Influenced by complex topography and significant climatic gradients, snow
94 cover, glaciers, and permafrost are widely distributed across the region.
95 Precipitation generally decreases from southeast to northwest, resulting in
96 significant variations in snowmelt accumulation, ablation, and runoff processes.
97 At the same time, ongoing climate warming has accelerated glacial retreat and
98 permafrost degradation, altering regional hydrological processes and runoff
99 formation conditions, and further increasing the uncertainty surrounding
100 snowmelt flood variability[11]. Furthermore, the uneven distribution of population,
101 infrastructure, and economic activities across the Tibetan Plateau results in
102 marked differences in socioeconomic vulnerability and adaptive capacity
103 among different regions. Consequently, areas with high physical flood hazard

do not necessarily correspond to areas with high comprehensive risk[12]. This spatial heterogeneity in natural environment and socioeconomic conditions makes the Tibetan Plateau a model region for studying the evolution of snowmelt flood hazard and its translation into comprehensive risk.

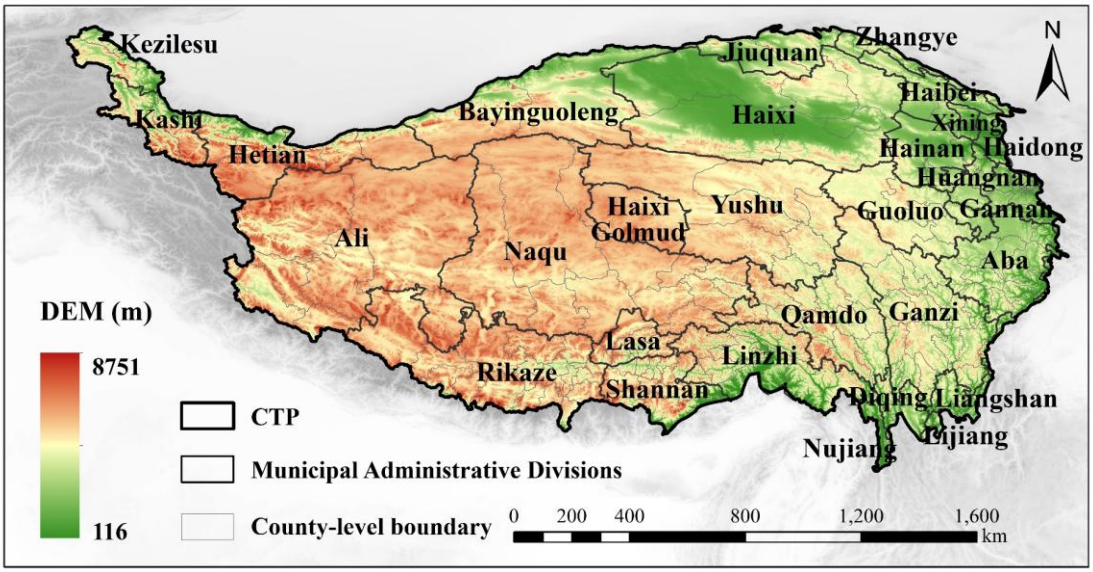

Figure 1 Study Area

3. Data and methods

3.1 Selection of snowmelt flood risk indicator and data sources

The indicator data for this study were primarily derived from satellite remote sensing and reanalysis products, spatial geographic data, the National Statistical Yearbook, and the Open Geospatial Information Platform (Table 1). Hydrometeorological and cryosphere data for 1980–2025 were primarily derived from two Global Land Data Assimilation System (GLDAS) product sets: GLDAS_CLSM025_D v2.0 (1980–2003)[13,14] and GLDAS_CLSM025_DA1_D

v2.2 (2004–2025)[15,16]. Daily precipitation and temperature data were obtained from the ERA5-Land reanalysis product[17]; topography[18,19], permafrost[20,21], population[22], and Tibetan Plateau boundary data[23,24] were sourced from the Tibetan Plateau Data Center (TPDC). Socioeconomic indicators were primarily compiled from the China Statistical Yearbook (NBS)[25,26,27] and the TPDC Social Vulnerability dataset[22], while built environment indicators were extracted from OpenStreetMap (OSM)[28]. To ensure spatial consistency among data from different sources, all spatial data were standardized to a grid resolution of 0.1° × 0.1°. In addition, this paper uses historical flood point data from TPDC[29,30] and Ground Source[31] to validate the final results.

Table 1 Snowmelt flood risk indicator system

Dimension	Code	Indicator	Unit
Hazard	H1	DEM (−)	m
	H2	Slope (−)	°
	H3	Topographic Wetness Index (+)	
	H4	Curvature (+)	m^{-1}
	H5	Distance to River (−)	km
	H6	Relative Height above Nearest River (−)	m
	H7	Soil Moisture (+)	kg m^{-2}
	H8	NDVI (−)	
	H9	Maximum 1-day Precipitation (+)	mm d^{-1}
	H10	Mean Annual Temperature (+)	°C
	H11	Permafrost Type (+)	categorical
	H12	Annual Maximum SWE (+)	mm
	H13	Annual Maximum Snowmelt Runoff (+)	mm d^{-1}
Exposure	E1	Population Density (+)	persons km^{-2}
	E2	GDP per Capita (+)	CNY $person^{-1}$
	E3	Grain Output per Capita (+)	kg $person^{-1}$
	E4	Oilseed Output per Capita (+)	kg $person^{-1}$
	E5	Livestock Stock Density (+)	head km^{-2}
	E6	POI Density (+)	counts km^{-2}
	E7	Urbanization Rate (+)	%

	E8	Traffic Density (+)	km km^{-2}
Sensitivity	S1	Share of agricultural, forestry, husbandry and fishery employment in rural employment (+)	%
	S2	Share of rural labor in total population (+)	%
	S3	Primary Industry Value-added Share (+)	%
	S4	Cultivated Land per Capita (+)	ha $person^{-1}$
	S5	Facility Agriculture Share (+)	%
	S6	Land-use Vulnerability Index (+)	
Adaptive Capacity	A1	Employment-to-Population Ratio (+)	%
	A2	Residential Savings per Capita (+)	CNY $person^{-1}$
	A3	Secondary & Tertiary Industry Share (+)	%
	A4	Hospital Beds (+)	beds per 10^4 persons
	A5	Fiscal Expenditure per Capita (+)	CNY $person^{-1}$
	A6	Loans per Capita (+)	CNY $person^{-1}$
	A7	Students-to-Population Ratio (+)	%
	A8	Road Network Density (+)	km km^{-2}
	A9	External Transport Accessibility (+)	
	A10	POI Diversity Index (+)	
	A11	Social Welfare Beds per Capita (+)	beds 10^4 $persons^{-1}$
	A12	Density of Above-designated-size Industrial Enterprises (+)	counts km^{-2}

3.2 Methods

3.2.1 Snowmelt flood extraction and trend analysis

Based on daily-scale snowmelt runoff time series, the annual maximum snowmelt runoff and its occurrence time were extracted at both the county level and the overall CTP scale. First, valid grid-based runoff data within the administrative boundaries of each county were spatially averaged to construct county-level daily snowmelt runoff time series; the same spatial averaging method was used to calculate the overall average daily snowmelt runoff time series for CTP.

The Annual Block Maxima method was used to extract annual snowmelt

flood characteristics[32]. Specifically, the annual maximum daily snowmelt runoff was used to characterize the annual flood peak, and its corresponding Day of Year (DOY; January 1 is Day 1) was recorded to characterize both the annual maximum snowmelt runoff volume and the timing of its occurrence.

Ordinary Least Squares (OLS) was used to perform a linear trend analysis on annual maximum snowmelt runoff and its onset date to quantify the rate of change of these two indicators over time[33]. Given potential discrepancies in data continuity between different versions of the GLDAS product, the study period was divided into two phases—1980–2003 and 2004–2025—with trend estimates conducted separately for each phase to minimize biases that might arise from switching between product versions.

3.2.2 AHP–CRITIC weighting integrated by game theory

This study employs a multi-criteria evaluation framework to construct an evaluation index comprising three dimensions: snowmelt flood hazard (H), exposure (E), and vulnerability (V). For the indicator systems of each dimension, the CRITIC method and the Analytic Hierarchy Process (AHP)[34] were used, respectively, to determine the objective and subjective weights. In particular, the CRITIC method measures the amount of objective information contained in each indicator by comprehensively considering the comparative strength of the indicators and the correlations among them, thereby determining their relative weights[35]. The AHP, on the other hand, determines subjective weights by

160 constructing a pairwise comparison matrix of indicator importance, thereby
161 incorporating expert knowledge and judgments of relative importance into the
162 evaluation system[36].

163 For exposure and vulnerability, a game-theory-based combined weighting
164 method was further employed to integrate subjective and objective weights,
165 determining the final indicator weights by balancing expert judgment with
166 statistical characteristics of the data[37]. For hazard assessment, the CRITIC
167 method was used to determine indicator weights. Vulnerability is further
168 characterized by a combination of sensitivity (S) and adaptive capacity (A).
169 Higher sensitivity increases system vulnerability, while stronger adaptive
170 capacity reduces it. Therefore, the vulnerability assessment simultaneously
171 considers the socioeconomic system's sensitivity to snowmelt flood as well as
172 its response and recovery capabilities.

173 Based on the final indicator weights, the standardized indicators were
174 weighted and aggregated to obtain composite indices for hazard, exposure, and
175 vulnerability, respectively.

176 Finally, the assessment results at the county level were spatialized onto a
177 unified raster grid, producing hazard, exposure, and vulnerability data with
178 consistent spatial resolution and spatial extent, thereby providing a foundation
179 for subsequent comprehensive risk assessments.

3.2.3 Integrated snowmelt flood risk assessment

The comprehensive snowmelt flood risk index is constructed based on three dimensions: hazard, exposure, and vulnerability. First, for the three assessment years—2000, 2010, and 2020—the raster data for each of the three dimensions were independently subjected to min–max normalization, converting valid pixels to the 0–1 range. Negative values and other invalid observations were excluded from the normalization and subsequent calculations.

$$X'_{i,t} = \frac{X_{i,t} - X_{min,t}}{X_{max,t} - X_{min,t}}$$

In the equation, $X_{i,t}$ and $X'_{i,t}$ represent the original and standardized values of the indicator for the (i)th grid cell in the (t)th year, respectively.

To balance expert judgment with the objective information contained in the data itself, this study employs a hybrid weighting framework that combines the Analytic Hierarchy Process (AHP), the CRITIC method, and game theory-based weighting. First, the AHP was used to construct a pairwise comparison matrix for the three-dimensional risk factors to determine the subjective weights for each dimension. In this process, relative importance was assigned to hazard over exposure and vulnerability, while exposure and vulnerability were treated as equally important to reflect the relative priorities of different risk dimensions in the comprehensive evaluation[36]. Second, the CRITIC method was employed to calculate objective weights by comprehensively considering the degree of

data variability across each dimension and its correlation with other dimensions, thereby measuring the relative information content contained in different risk dimensions[35].

Subsequently, a game-theory-based combined weighting method was used to integrate the AHP subjective weights with the CRITIC objective weights. By optimizing the linear combination coefficients of different weight vectors, a relatively balanced combination scheme was sought between the two weighting results, thereby reducing the reliance of the final weights on individual subjective judgments or statistical characteristics of the data[37]. The aforementioned combined weighting process was conducted independently for each of the three evaluation years. Based on this, the annual combined weights obtained for 2000, 2010, and 2020 were averaged arithmetically and renormalized to obtain unified dimension weights applicable to all three evaluation years, thereby ensuring a consistent weighting basis for comprehensive risk assessments across different time periods.

The comprehensive snowmelt flood risk index is calculated using a weighted linear superposition method:

$$R_{i;t} = \omega_H H^*_{i;t} + \omega_E E^*_{i;t} + \omega_V V^*_{i;t}$$

where $R_{i;t}$ is the integrated risk score at grid cell i in year t; $H^*_{i;t}$, $E^*_{i;t}$ and $V^*_{i;t}$ are the normalized hazard, exposure and vulnerability indices; and ω_H, ω_E and ω_V are the common component weights. Risk was calculated

only for cells where all three components had valid values.

Finally, using static socioeconomic data and hazard data from each period, the composite risk scores for the three periods were range-normalized, thereby generating composite risk spatial distribution maps for the periods 1991–2000, 2001–2010, and 2011–2020. Consequently, the resulting risk maps reflect the relative spatial patterns of risk within each assessment year, rather than absolute risk levels that are directly comparable across different years. The analysis of temporal changes primarily involves a comprehensive interpretation that combines the spatial distribution and changes in the hierarchical structure of the composite risk with the spatiotemporal changes in the three constituent dimensions: hazard, exposure, and vulnerability.

3.2.4 Identification of key risk factors using CatBoost and SHAP

The CatBoost model was used to establish a nonlinear relationship between the comprehensive snowmelt flood risk index and various risk indicators. CatBoost is an ensemble learning algorithm based on gradient-boosted decision trees that reduces prediction bias and improves the model's predictive performance through strategies such as ordered boosting[38]. With the comprehensive risk index as the response variable and the indicators under the dimensions of hazard, exposure, vulnerability, and adaptive capacity as predictor variables, a unified ensemble model was constructed based on

county-level samples to identify the complex relationships between different risk indicators and the comprehensive risk. We further introduce the SHapley Additive exPlanations (SHAP) method to interpret the model's predictive results. Based on Shapley values from game theory, this method decomposes the model's output into the contributions of individual predictors, thereby providing a quantitative explanation of the model's predictions[39].

The mean absolute SHAP value is used to measure the importance of individual indicators, and the SHAP contributions at the indicator level are aggregated to the risk dimension to compare the relative contributions of hazard, exposure, vulnerability, and adaptive capacity to the prediction of comprehensive risk. The SHAP explanation method for tree models further supports the transition from local prediction explanations to global feature importance analysis[40]. At the same time, the analysis results were aggregated separately by sub-basin and assessment year to reveal the spatial heterogeneity and temporal variations in the relative importance of risk factors across different geographic units and time periods. Furthermore, SHAP dependency analysis was used to identify association patterns and potential nonlinear characteristics between key indicators and model prediction results.

3.2.5 Sensitivity and robustness analysis

To test the comprehensive risk index's tolerance for uncertainty in indicator weights, this study conducted a single-factor weight perturbation sensitivity

analysis for three base years (2000, 2010, and 2020)[41]. Based on the SHAP global importance analysis of all 39 H–E–V indicators (Section 5.2 of the Discussion)[39], the three indicators with the highest importance rankings across the entire watershed were selected—S01, S04, and H10—as the targets for perturbation. The weights of each indicator within its respective subsystem were increased or decreased by 20%; after perturbation, the weights of all indicators within that subsystem were re-normalized so that their sum equaled 1, while the dimension weights remained unchanged.

During classification, four internal breakpoints were determined using the Jenks natural breakpoint method (k = 5)[42] based on the continuous R-values of the baseline scenario, and this set of thresholds was applied uniformly to all perturbation scenarios. Risk levels were classified into five categories: Very Low, Low, Moderate, High, and Very High, with high-risk pixels defined as those with a risk level ≥ 4. Within the range of pixels common to all five scenarios (masked by the baseline hazard raster), the risk levels of the perturbation scenarios were compared pixel-by-pixel with those of the baseline scenario. Let N_{total} denote the total number of common valid pixels, N_{same} denote the number of pixels with consistent risk levels between the baseline and perturbation scenarios, and the number of pixels with a changed risk level is $N_{changed}$ (such that $N_{same} + N_{changed} = N_{total}$). The numbers of high-risk pixels under the baseline and perturbed scenarios are N_{base}^{high} and N_{pert}^{high}, respectively. The three soundness

indicators are defined as follows:

$$Agreement = \frac{N_{same}}{N_{total}} \times 100\%$$

$$Transition\ Rate = \frac{N_{changed}}{N_{total}} \times 100\%$$

$$High - risk\ Pixel\ Change = \frac{N_{pert}^{high} - N_{base}^{high}}{N_{base}^{high}} \times 100\%$$

4. Results

4.1 Spatiotemporal changes in snowmelt flood

The annual maximum snowmelt runoff (AMF) in CTP exhibits distinct phased variations in both the timing of occurrence and the magnitude of the flood (Fig. 2). Based on the regional average time series (Fig. 2e), the onset dates of AMF showed a trend toward earlier occurrence in both time periods; however, the rate of advance slowed from 1.50 d/a during 1980–2003 to 0.54 d/a during 2004–2025, representing a decrease of approximately 64%. At the same time, interannual variability in onset dates narrowed after 2004. AMF magnitude (Fig. 2f) showed a slight increasing trend in both periods, but the estimated growth rate decreased from 0.03 mm/10a to 0.01 mm/10a. Furthermore, the overall magnitude has declined since 2004, with signs of a further decline since 2015. Spatially, the onset dates of AMF exhibit distinct regional variations (Fig. 2a, c). From 1980 to 2003, the trend toward earlier onset was primarily concentrated in the Nagqu–Lhasa area of the central

Plateau, while most of Qinghai, western Sichuan, and eastern Tibet showed a predominant trend toward later onset. From 2004 to 2025, the region where the onset date occurred earlier expanded eastward from the central Plateau, while the region where the onset date occurred later shrank significantly, primarily confined to Ali and localized areas in the northwestern Plateau. Unlike the onset dates, the spatial variation in AMF magnitude gradually shifted from an early pattern of increasing values in the west and decreasing values in the east to a widespread, slight decrease (Fig. 2b, d). From 1980 to 2003, areas of increase were mainly concentrated in western Tibet (Ali Prefecture), while southeastern Tibet and the Hengduan Mountains showed a predominantly decreasing trend; from 2004 to 2025, the original western center of increase weakened significantly, and most of the Plateau exhibited a slight decreasing trend, with only eastern Qinghai and localized areas in western Sichuan retaining relatively distinct signals of increase. After 2004, the AMF of CTP exhibited characteristics of a continuous advance in the onset date—though at a slowing rate—as well as a slowing growth in runoff volume and a narrowing spatial extent of increase.

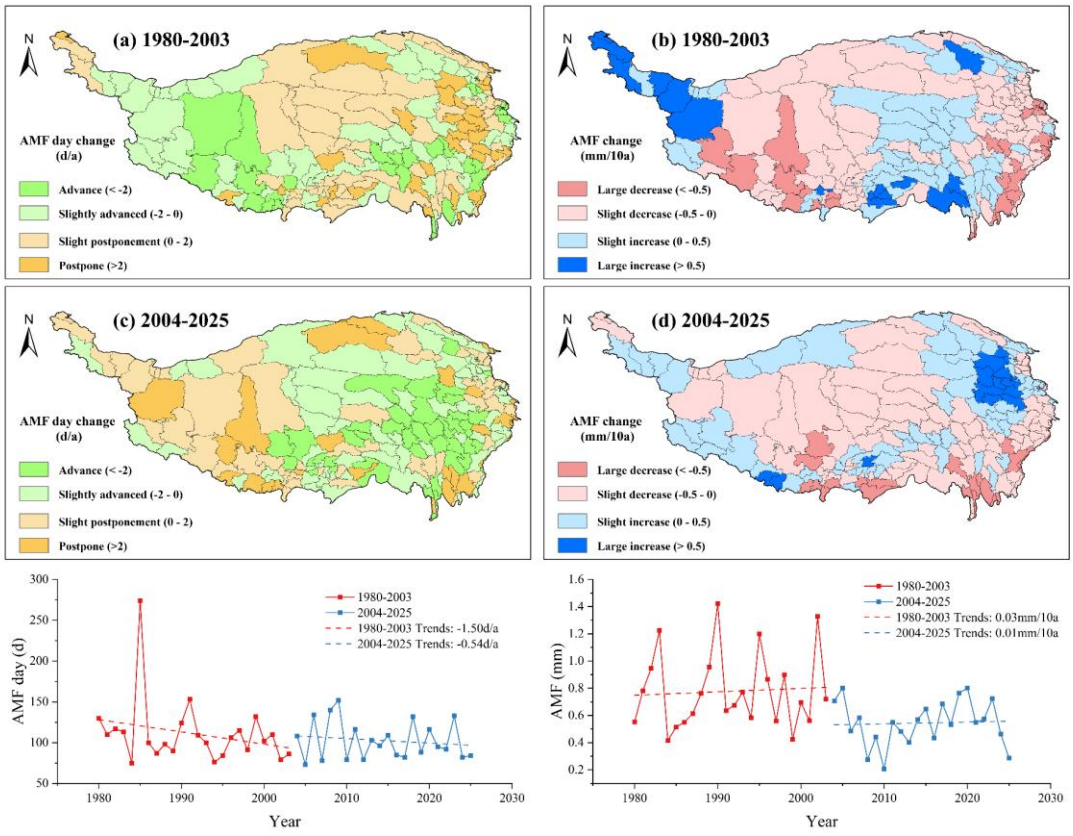

Figure 2 Spatiotemporal Distribution and Interannual Variations of AMF in CTP from 1980 to 2025 (Based on the Merging of Two Datasets)

4.2 Spatial patterns of snowmelt flood hazard

The CRITIC weights of disaster-causing factors showed significant differences between the two periods (Table 2). From 1980 to 2003, the combined weight of H13, H11, and H7 was 0.366, representing a relatively important combination of indicators in early hazard assessments. From 2004 to 2025, H5, H11, and H3 became the three indicators with the highest weights, while H13 dropped from first to tenth place. At the same time, the weight of H8 increased, indicating a greater relative contribution of vegetation indicators to the spatial differentiation of hazard risk in the later period. The weighting

structure of the hazard assessment indicators shifted from a relative emphasis on early-stage snowmelt runoff, permafrost, and soil moisture indicators to a relative emphasis on late-stage topographic-hydrological and permafrost indicators.

Table 2 Weights of AMD Risk Assessment Factors in the Two CTP Cohorts

Factor	1980-2003	2004-2025
Qsm	0.131	0.059
Permafrost	0.126	0.134
Distance to River	0.121	0.135
SM	0.109	0.094
TWI	0.090	0.099
DEM	0.079	0.087
Relative Height	0.073	0.081
NDVI	0.064	0.085
Temp_Mean	0.063	0.067
Slope	0.059	0.065
Curvature	0.035	0.039
Rx1day	0.027	0.031
SWEmax	0.023	0.024

The risk index constructed based on the above weights exhibits distinct spatial heterogeneity and temporal variations (Fig. 3). Between 1980 and 2003, areas with medium to high risk covered the remaining 57%, located mainly along the eastern and southern margins (Fig. 3a). Of the 20 historical flood sites, 55% were located in high- or very high-risk zones, with an average risk level score of 3.60 (Fig. 3c). From 2004 to 2025, extremely low-risk zones accounted for approximately 16% of the study area, while extremely high-risk zones accounted for 23%. High- and extremely high-risk zones are notably present along the southern and southeastern margins, with some high-risk patches

forming a more spatially connected pattern (Fig. 3b). Of the 1,131 flood points, 90.1% were located in high- or very high-risk zones, and 68.3% were in extremely high-risk zones; the average risk level score was 4.53 (Fig. 3d).

Two patterns emerge when watershed scores are examined jointly by baseline level and change magnitude (Fig. 3e). First, the basins with the largest increases are precisely those with the lowest baseline scores: the Ganges (2.08 → 3.43, +1.35), the Brahmaputra (2.67 → 3.64, +0.96), and the Indus (2.10 → 2.97, +0.87) all rose by nearly one or even more than one full risk level. Second, the river basins with the highest baseline risk—the Yellow (4.11), Yangtze (3.94), and Mekong (3.97) in the eastern monsoon river source regions—showed minimal changes or even slight decreases (−0.07 to −0.18). The arid, the Inner Plateau and the Salween remained in the middle range during both periods, with changes not exceeding 0.22. These changes collectively reshaped the spatial gradient of snowmelt flood risk: the earlier east-west contrast of “high in the east, low in the west” has weakened, while the basins on the southern slopes of the Himalayas have shifted from the lowest risk category to the medium-to-high risk category.

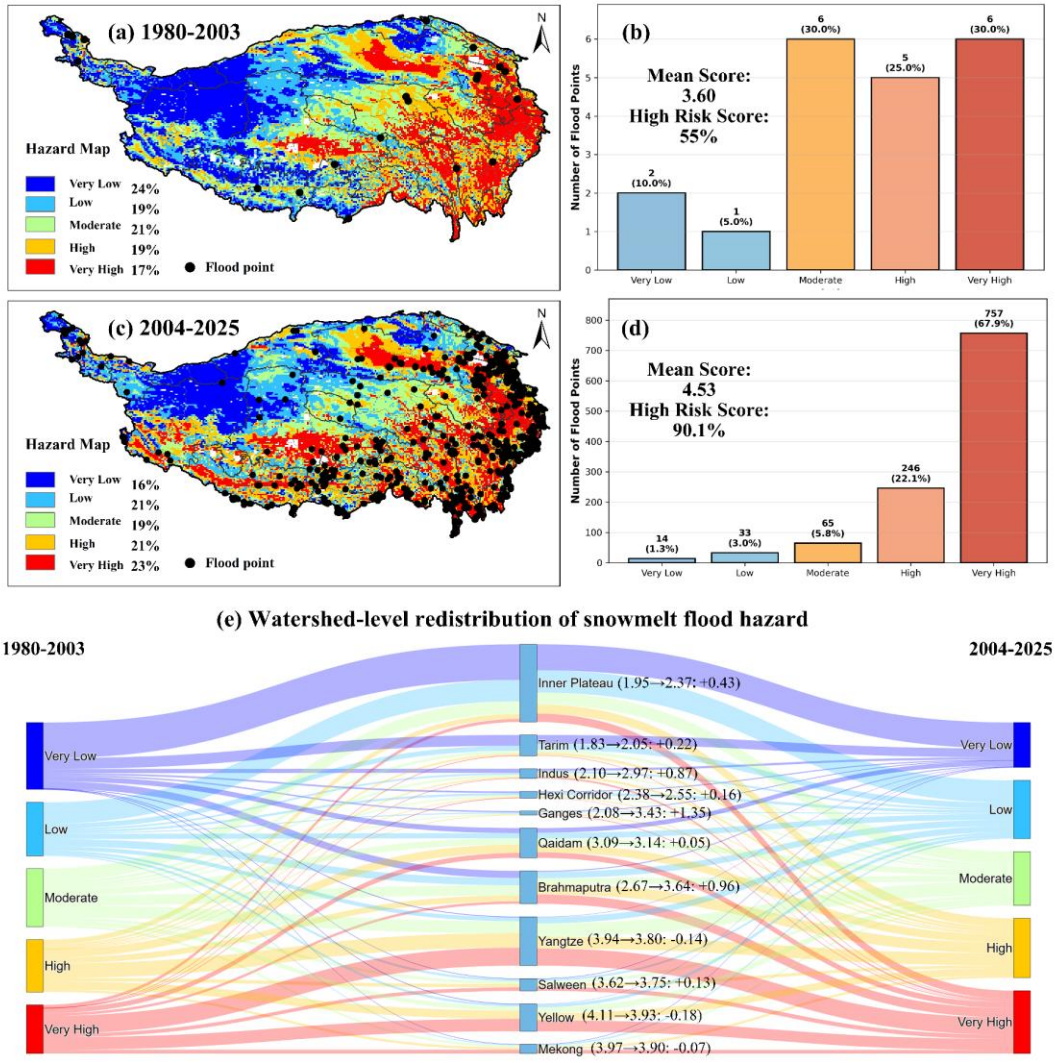

Figure 3 Spatiotemporal Evolution and Watershed-Scale Variation of Snowmelt Flood Hazards in the CTP.

4.3 Evolution of snowmelt flood vulnerability

From 2000 to 2020, CTP snowmelt flood vulnerability showed an overall downward trend, with the spatial pattern gradually shifting from widespread clusters of high vulnerability in the core regions to a coexistence of residual localized high vulnerability and the expansion of low vulnerability in peripheral areas (Fig. 4a–c). The proportion of areas with high and extremely high

vulnerability decreased from 43.5% in 2000 to 19.3% in 2020, while the proportion of areas with low and extremely low vulnerability increased from 36.9% to 57.1%. In 2000, areas of high vulnerability were primarily concentrated in the interior of the Qiangtang region in northern Tibet and the Ali Prefecture, extending upstream along the Brahmaputra. By 2010, the high-vulnerability patches in these areas had noticeably shrunk, while low-vulnerability areas gradually expanded in the Hehuang Valley, western Sichuan, and the Lhasa–Shigatse–Nyingchi region. By 2020, the areas of extremely high vulnerability had further contracted to a few counties in the heart of the Qiangtang, while areas of low and extremely low vulnerability formed a more continuous distribution across the eastern Plateau, southern river valleys, and the Hengduan Mountains.

Changes at the watershed scale further reveal regional differences in the decline in vulnerability (Fig. 4d). River basin vulnerability shows a downward trend, but the magnitude of the decline is closely related to the initial baseline level. The river basins with the highest baseline values in 2000—the Indus (0.74) and the Inner Plateau (0.74)—experienced the largest declines: the Indus River decreased by 0.24, and the Inner Plateau decreased by 0.10. Basins with intermediate baseline levels—ranging from approximately 0.45 to 0.49—decreased further by 0.10–0.17, while the Qaidam Basin (0.34), which had the lowest baseline, remained essentially unchanged (+0.01). Over time, the

decline was not uniform: changes in most basins were gradual from 2000 to 2010, but the decline accelerated significantly from 2010 to 2020. The net effect was a convergence of vulnerability across basins—basins with initially high vulnerability improved the fastest, while those with initially low vulnerability tended to stabilize— — which is consistent with the overall trends reflected in the pie chart: the proportion of basins with extremely high vulnerability decreased from 21.2% in 2000 to 1.5% in 2020, while the proportion of basins with extremely low vulnerability increased from 8.6% to 23.5% (Fig. 4a-c).

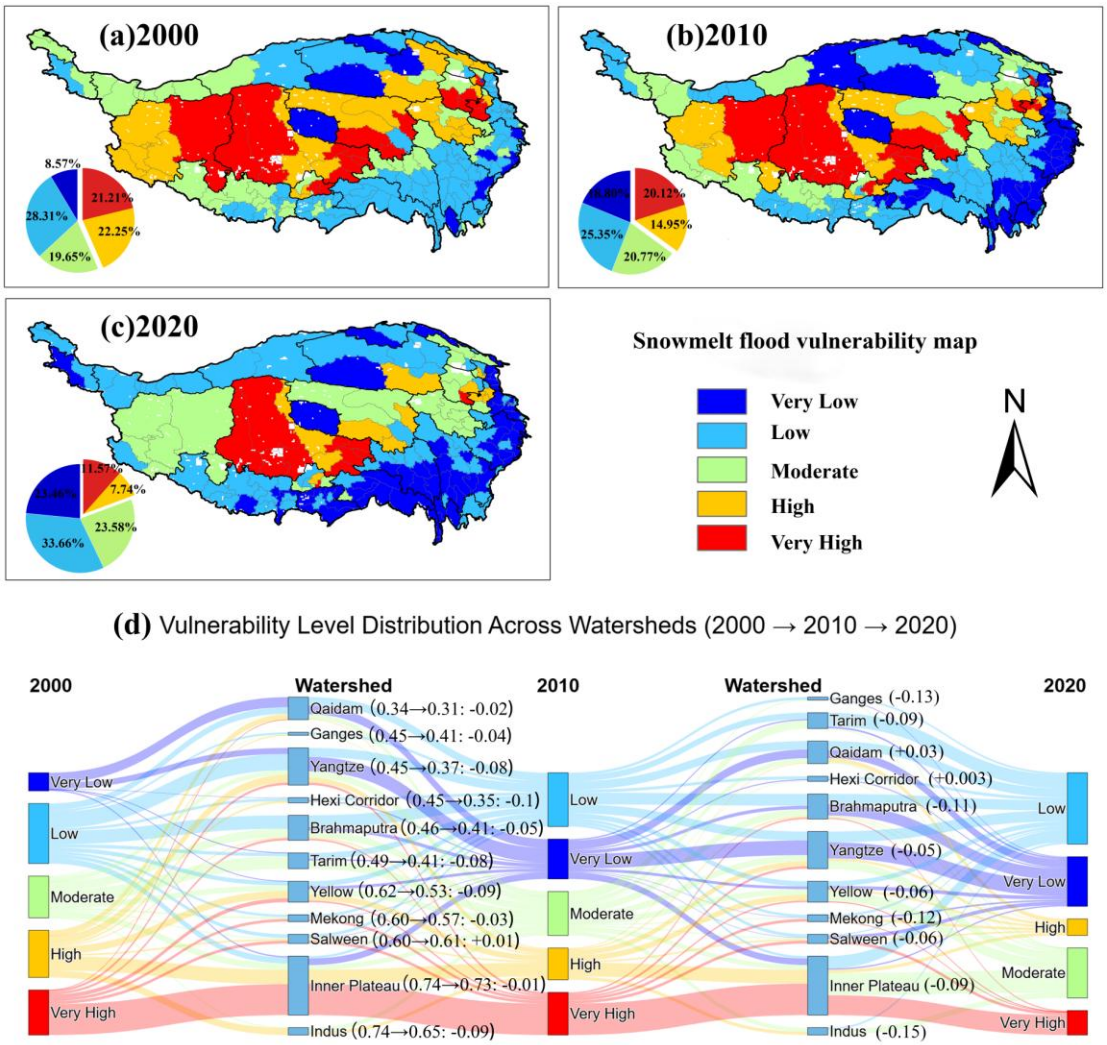

Figure 4 Spatiotemporal Evolution and Watershed-Scale Redistribution of

4.4 Dynamic changes in integrated snowmelt flood risk

In the comprehensive risk assessment, the final combined weights for hazard (H), exposure (E), and vulnerability (V) were 0.453, 0.274, and 0.273, respectively, with hazard carrying a relatively higher weight. A unified assessment system was constructed based on the average combined weights across the three periods, further revealing the spatiotemporal evolution characteristics of the comprehensive risk of CTP snowmelt flood from 2000 to 2020 (Fig. 5).

Geographically, the comprehensive risk overall exhibits a distribution pattern characterized by “high risk in the southeast and low risk in the northwest.” High-risk areas are primarily concentrated on the southern slopes of the Himalayas, the eastern section of the Nyenchen Tanglha Mountains, the Hengduan Mountains, and the eastern Qilian Mountains. Temporally, the composite snowmelt-flood risk index exhibited an inverted-U trajectory between 2000 and 2020 (Fig. 5a–c). From 2000 to 2010, the proportion of high- and extremely high-risk areas rose from 36.6% to 39.1%, while the proportion of low- and extremely low-risk areas fell from 35.5% to 28.7%. By 2020, the proportion of high- and extremely high-risk areas had dropped to 22.8%, and the proportion of low- and extremely low-risk areas had risen to 46.4%.

Changes at the watershed scale further reveal regional differences in the

evolution of the comprehensive risk index (Fig. 5d). From 2000 to 2010, risks increased in most river basins, with the increases concentrated in basins with lower baseline levels—the Ganges (+0.08), the Brahmaputra (+0.06), and the Inner Plateau (+0.05); whereas in the headwaters of eastern rivers with higher baseline levels (the Yellow River −0.03, the Yangtze −0.03), changes were minimal or even declined. From 2010 to 2020, this pattern reversed: risks in nearly all river basins decreased simultaneously (from −0.03 to −0.08), with no apparent correlation to baseline levels. The net change from 2000 to 2020 was therefore primarily driven by the eastern rivers, which had higher initial baseline levels (Yellow −0.08, Yangtze −0.07, Mekong −0.06), while the southern and western river basins, which had lower baseline levels, essentially returned to their starting points (Ganges 0.00, Salween 0.00, Brahmaputra −0.01). The overall effect was a two-stage convergence: during the upward phase, basins with low baseline values caught up, while during the downward phase, all regions declined simultaneously, resulting in a spatial contrast in 2020 that was weaker than that in 2000.

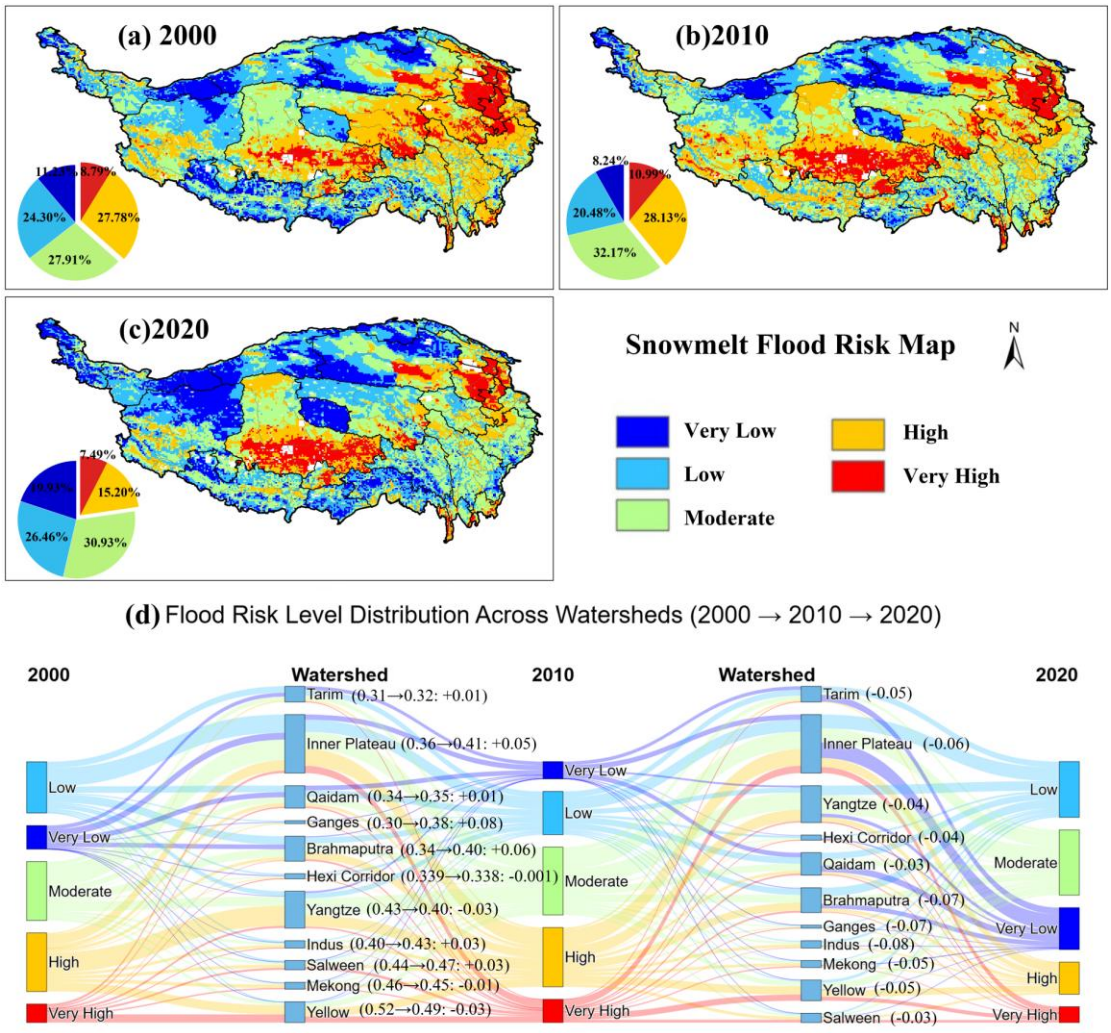

Figure 5 Spatiotemporal Evolution and Watershed-Scale Redistribution of Integrated Snowmelt Flood Risks in the CTP

5. Discussion

5.1 Divergence between hazard and integrated risk

To reveal the spatial relationship between physical hazards and social vulnerability, this study employed a bivariate combination analysis to identify the primary spatial combinations of snowmelt flood hazards and social vulnerability in CTP, as well as their variations (Fig. 6). From 2000 to 2020, the

proportion of hazard-dominated areas (high hazard–low vulnerability) increased from 18.07% to 28.99%, while that of low-hazard–low-vulnerability areas rose from 11.53% to 18.88%; At the same time, the proportion of “double-high” regions (high hazard–high vulnerability) decreased from 12.22% to 7.87%, while the proportion of vulnerability-dominated regions (low hazard–high vulnerability) dropped significantly from 21.18% to 6.95%. This change indicates that the spatial combination of hazard and social vulnerability underwent a marked adjustment during the study period; the two did not change in tandem, and the regional risk pattern gradually exhibited more pronounced hazard-dominated characteristics.

This spatial variation may be related to differences in natural environmental processes and socioeconomic conditions. On the one hand, different regions of the Tibetan Plateau exhibit significant variations in climatic conditions, snowmelt processes, and permafrost distribution; warming and changes in permafrost freeze-thaw cycles can alter the spatial distribution of flood risk by influencing soil moisture transport, runoff formation, and convergence processes[11,43]. On the other hand, social vulnerability is not only influenced by disaster intensity but is also closely related to household livelihood strategies, economic capital, and adaptive capacity. Existing surveys of plateau farmers have found that livelihood structures and household capital endowments are key factors influencing rural social vulnerability[44,45], while external interventions

may also influence farmers' adaptive capacity in coping with climate risks[46]. Therefore, changes in the proportion of hazard-vulnerability combinations may reflect a lack of synchronization between the spatial patterns of natural hazards and the evolution of social vulnerability; however, the specific causal relationship cannot be determined solely based on the spatial combination of these two variables.

Bivariate analysis revealed a spatial mismatch between physical hazards and social vulnerability: the expansion of high-hazard areas was not accompanied by a corresponding increase in areas characterized by both high physical hazards and high social vulnerability, while areas dominated by social vulnerability clearly contracted. This suggests that identifying snowmelt flood risks based solely on physical hazards may not accurately reflect the comprehensive risk differences across different regions. Risk assessment and management should further integrate hazard, exposure, and social vulnerability to identify areas with high natural hazards but low social vulnerability, as well as areas with relatively low natural hazards but high social vulnerability, thereby enabling the formulation of region-specific risk management strategies.

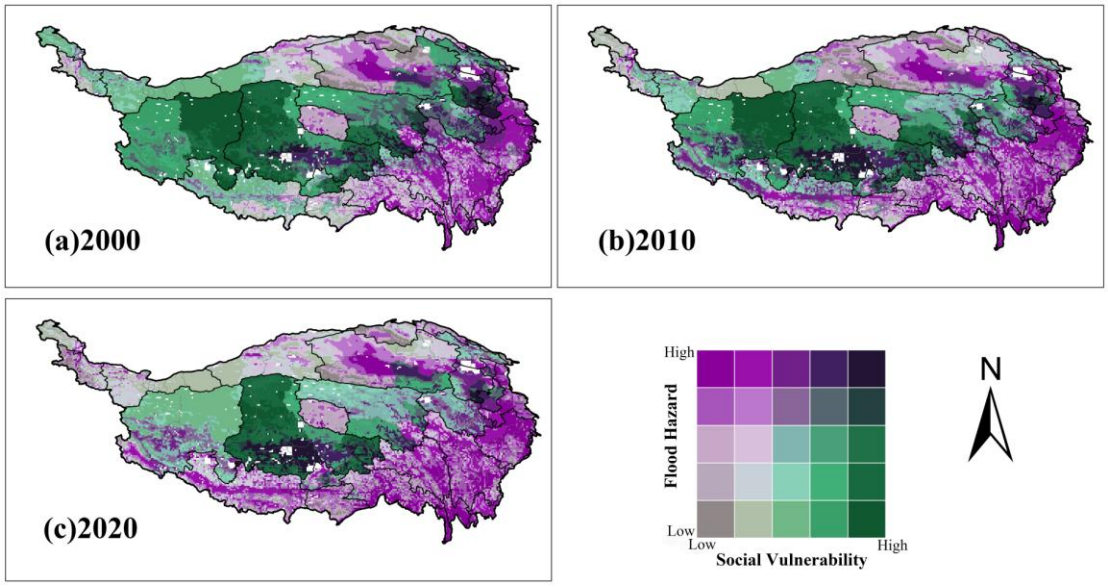

Figure 6 Bivariate mapping of flood hazard and social vulnerability, 2000–2020. The horizontal axis represents social vulnerability (low → high); the vertical axis represents flood hazard (low → high).

5.2 Relative contributions of individual indicators to composite risk

CatBoost–SHAP analysis further revealed the dominant dimensions of the comprehensive snowmelt flood risk in CTP and their regional variations (Fig. 7). From 2000 to 2020, the average relative contribution of hazard in the 11 sub-basins decreased from 41.2% to 36.7%, that of vulnerability decreased from 26.1% to 22.6%, while that of adaptive capacity increased from 21.4% to 30.1%; exposure remained at a relatively low level (approximately 11%) throughout the period. These changes indicate that the model's explanation of spatial variations in comprehensive risk has gradually shifted from hazard and vulnerability toward adaptive capacity; however, this does not imply that

physical hazards have actually diminished or that adaptive capacity has necessarily improved. Meanwhile, the Tarim River basin has consistently exhibited a high contribution from hazard (approximately 48%–50%), while the Brahmaputra, Ganges, and Yangtze River basins have shown a relatively prominent contribution from adaptive capacity, reflecting significant heterogeneity in the risk profiles of different sub-basins.

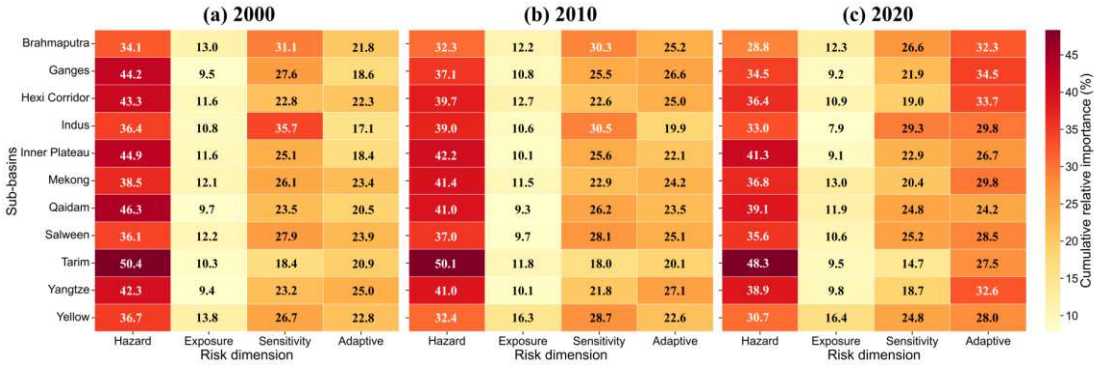

Figure 7 Relative importance of snowmelt-flood risk dimensions across sub-basins of CTP, 2000–2020

At the level of specific indicators (Fig. 8), the proportion of rural agricultural employment (S1) ranked first in 8 of the 11 sub-basins, with a relative importance of approximately 11%–13.5%, highlighting the significance of the agricultural livelihood structure in explaining spatial variations in social vulnerability on the plateau. Previous studies have also indicated that livelihood patterns, household economic status, and capital endowment are closely associated with rural social vulnerability on the Tibetan Plateau[44,45]. Regional differences are further reflected in variations in the dominant indicators: in inland basins strongly influenced by westerlies, distance from rivers (H5),

temperature (H10), and permafrost-related factors are particularly prominent, reflecting the influence of topography, hydrology, and permafrost processes on spatial variations in flood risk[11,43]; whereas in some monsoon-influenced areas, resilience indicators such as external transportation accessibility (A9) and financial capital (A6, A2) carry greater relative importance, which may be related to access to public services, resource allocation, and post-disaster recovery conditions[46,47]. In contrast, exposure indicators rarely appear among the top ten in each watershed, suggesting that their relative explanatory contribution to spatial variations in comprehensive risk is low in the current model; however, this does not imply that population and economic exposure are unimportant for actual disaster losses.

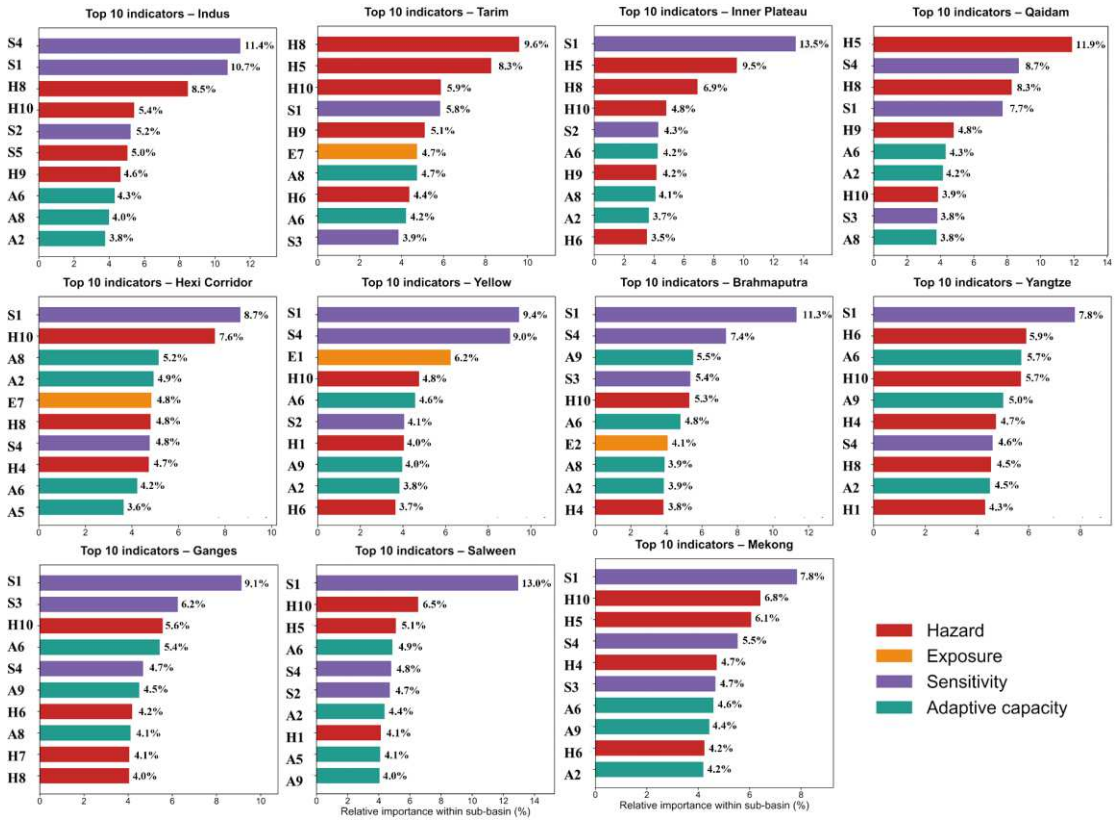

Figure 8 Top-ten risk indicators across sub-basins of CTP

5.3 Sensitivity and robustness of composite risk assessment

Comprehensive risk assessments are inevitably influenced by the selection of indicators, the assignment of weights, and the associated uncertainties—particularly for dimensions that are difficult to quantify directly, such as socioeconomic vulnerability. Different combinations of weights may alter the final spatial assessment results. Therefore, sensitivity analysis is a crucial method for evaluating the reliability and spatial robustness of comprehensive assessment results[48,49]. In this study, based on the CatBoost–SHAP global importance ranking in Section 5.2, S1, S4 and H10 were selected for ±20% weight perturbations. The results show that the consistency rate of risk levels across the 18 perturbation scenarios ranged from 96.95% to 100.00% (Table 3), and the spatial locations and overall distribution patterns of the primary high-risk areas remained largely stable (Fig. 9). This result indicates that the spatial variation in the comprehensive snowmelt flood risk of CTP is not dominated by the weight settings of a few indicators. This is consistent with findings from existing flood vulnerability studies, which suggest that while changes in weights may affect spatial evaluation results with regional variations, the overall pattern may remain stable[49,50].

Table 3 Sensitivity Analysis of Phase III Risk Assessment Results Under ±20% Perturbations of Key Factors

year	Perturbation	Agreement Rate (%)	Transition Rate (%)	High Risk Pixel Change (%)

2000	S1 +20%	99.06	0.94	0
	S1 -20%	98.60	1.40	2.48
	S4 +20%	98.60	1.40	1.10
	S4 -20%	99.36	0.64	-0.02
	H10 +20%	98.23	1.77	0.86
	H10 -20%	99.99	0.01	-0.02
2010	S1 +20%	96.95	3.05	0
	S1 -20%	98.78	1.22	1.77
	S4 +20%	99.50	0.50	0.56
	S4 -20%	99.50	0.50	0.56
	H10 +20%	99.00	1.00	0.56
	H10 -20%	100.00	0.00	0.00
2020	S1 +20%	99.60	0.40	-0.02
	S1 -20%	97.06	2.94	0.36
	S4 +20%	98.29	1.71	0.36
	S4 -20%	98.09	1.91	4.80
	H10 +20%	98.29	1.71	0.36
	H10 -20%	99.99	0.01	-0.02

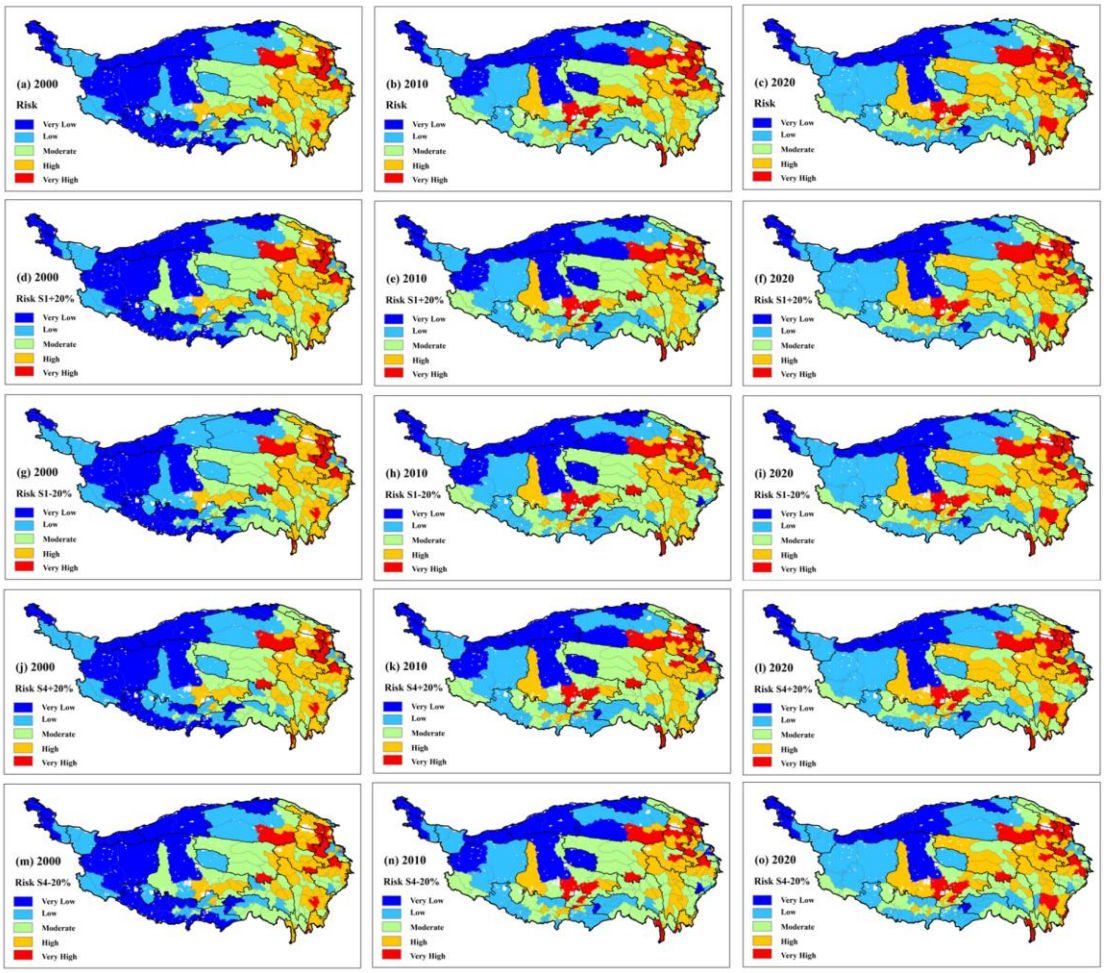

Figure 9 Snowmelt Flood Risk Assessment: OAT Sensitivity Analysis—Spatial Patterns of the Baseline and After ±20% Perturbations to Factors S1 and S4

Although the overall pattern exhibits a high degree of stability, different indicators still respond differently to weighting adjustments (Table 3). S1 is relatively sensitive to changes in risk levels; a 20% increase in weighting in 2010 and a 20% decrease in 2020 resulted in conversion rates of 3.05% and 2.94%, respectively; In contrast, a 20% reduction in the weight of S4 in 2020 led to a 4.80% increase in the number of high-risk pixels—the largest increase among all scenarios. By comparison, the overall impact of perturbations on H10 was relatively minor; specifically, when its weight was reduced by 20%, the

consistency rate of risk levels across the three years remained close to 100%. This discrepancy may be related to the attributes characterized by the indicators and their spatial distribution: S1 and S4 reflect agricultural livelihood structures and land resource conditions that exhibit strong regional heterogeneity, which may influence changes in the boundaries of local vulnerability levels[50,51]; whereas the impact of H10 is constrained by the combined effects of other hazard and vulnerability factors.

Weight perturbations did not alter the primary spatial patterns of the comprehensive snowmelt flood risk assessed by CTP, indicating that the evaluation framework developed in this study exhibits good weight robustness. However, this stability primarily reflects the response to weight perturbations within the established indicator system and does not imply that the evaluation results are free from other uncertainties. In the future, it will be necessary to further validate the reliability of the comprehensive risk assessment results by incorporating actual flood disaster records and different model settings.

6. Conclusion

This study developed a comprehensive evaluation framework that integrates hazard, exposure, vulnerability, and interpretable machine learning methods to assess the dynamic risks of snowmelt flood on CTP. The study reached the following four main conclusions.

First, snowmelt flood on CTP exhibits significant spatiotemporal heterogeneity; both the intensity and timing of flood peaks showed varying degrees of change between the two periods of 1980–2003 and 2004–2025. These changes reveal the dynamic characteristics of snowmelt flood hazards and indicate that regional risk assessments must fully account for the temporal variability of these hazards.

Second, the comprehensive risk landscape is not a simple spatial mapping of physical hazards. From 2000 to 2010, the proportion of high-risk and extremely high-risk areas increased; however, their combined proportion decreased from 39.1% in 2010 to 22.7% in 2020. At the same time, the proportion of high-vulnerability and extremely high-vulnerability areas declined significantly from 43.5% in 2000 to 19.3% in 2020. These divergent spatial changes indicate that, in addition to physical hazards, socioeconomic conditions and exposure levels also play a significant role in shaping the regional comprehensive risk landscape.

Third, the CatBoost–SHAP analysis revealed significant differences in the relative importance of the 11 key basin risk indicators. Risk-related factors continue to make a significant contribution, while socioeconomic vulnerability and adaptive capacity also play a role that cannot be overlooked. The prominent performance of indicators related to the rural agricultural workforce in most basins further underscores the importance of livelihood-related factors

in explaining regional differences in risk.

Fourth, OAT sensitivity analysis indicates that, under moderate weight perturbations, the classification of risk spaces remains highly consistent, supporting the robustness of the comprehensive assessment results.

Overall, this study has advanced the evaluation of snowmelt flood risks on the Chinese part of the Tibetan Plateau from a single perspective centered on physical hazards toward a comprehensive understanding of risk that integrates both natural and socioeconomic dimensions. The research findings can provide a scientific basis for sub-basin risk management and the formulation of targeted adaptation strategies on the Tibetan Plateau.

Acknowledge

This study was supported by the National Key Research and Development Program of China (2024YFF0808602), the Science and Technology Projects of Xizang Autonomous Region, China (XZ202601ZD0014–09), Gansu Key Research and Development Program (26YFWA001), the program of the State Key Laboratory of Cryospheric Science and Frozen Soil Engineering CAS (CSFSE-FX-2501).

References

1. Hock, R., Rasul, G., Adler, C. et al. (2019). High mountain areas. In The

626 Ocean and Cryosphere in a Changing Climate, H.-O. Pörtner, D.C. Roberts, V.
627 Masson-Delmotte et al., eds. (Cambridge University Press), pp. 131–202.
628 DOI:10.1017/9781009157964.004.
629 2. Guo, Y., Yang, Y., Yang, D. et al. (2025). Warming leads to both earlier
630 and later snowmelt floods over the past 70 years. Nat. Commun. 16:3663.
631 DOI:10.1038/s41467-025-58832-0.
632 3. Adler, C., Wester, P., Bhatt, I. et al. (2022). Cross-Chapter Paper 5:
633 Mountains. In Climate Change 2022: Impacts, Adaptation and Vulnerability, H.-
634 O. Pörtner, D.C. Roberts, M. Tignor et al., eds. (Cambridge University Press),
635 pp. 2273–2318. DOI:10.1017/9781009325844.022.
636 4. Cui, P. and Jia, Y. (2015). Mountain hazards in the Tibetan Plateau:
637 Research status and prospects. Natl. Sci. Rev. 2:397–399.
638 DOI:10.1093/nsr/nwv061.
639 5. Ye, T., Shi, P. and Cui, P. (2023). Integrated disaster risk research of the
640 Qinghai-Tibet Plateau under climate change. Int. J. Disaster Risk Sci. 14:507–
641 509. DOI:10.1007/s13753-023-00510-0.
642 6. Yang, L., Ma, J., Wang, X. et al. (2022). Hydroclimatology and
643 hydrometeorology of flooding over the eastern Tibetan Plateau. J. Geophys.
644 Res. Atmos. 127: e2022JD037097. DOI:10.1029/2022JD037097.
645 7. Niu, L., Wang, J., Li, H. et al. (2025). Weakened snowmelt contribution
646 to floods in a climate-changed Tibetan basin. Water 17:507.

DOI:10.3390/w17040507.

8. Wang, S., Zhou, L. and Wei, Y. (2019). Integrated risk assessment of snow disaster over the Qinghai-Tibet Plateau. Geomatics Nat. Hazards Risk 10:740–757. DOI:10.1080/19475705.2018.1543211.

9. Sun, S., Zhang, Q., Xu, Y. et al. (2021). Integrated assessments of meteorological hazards across the Qinghai-Tibet Plateau of China. Sustainability 13:10402. DOI:10.3390/su131810402.

10. Bibi, S., Wang, L., Li, X. et al. (2018). Climatic and associated cryospheric, biospheric, and hydrological changes on the Tibetan Plateau: A review. Int. J. Climatol. 38: e1–e17. DOI:10.1002/joc.5411.

11. Gao, H., Wang, J., Yang, Y. et al. (2021). Permafrost hydrology of the Qinghai-Tibet Plateau: A review of processes and modeling. Front. Earth Sci. 8:576838. DOI:10.3389/feart.2020.576838.

12. Ji, Q., Yang, J., Wang, C. et al. (2021). The risk of the population in a changing climate over the Tibetan Plateau, China: Integrating hazard, population exposure and vulnerability. Sustainability 13:3633. DOI:10.3390/su13073633.

13. Li, B., Beaudoing, H. and Rodell, M. (2018). GLDAS Catchment Land Surface Model L4 daily 0.25×0.25 degree, Version 2.0 [Data set]. NASA Goddard Earth Sciences Data and Information Services Center. DOI:10.5067/LYHA9088MFWQ.

668 14. Li, B., Rodell, M., Sheffield, J. et al. (2019). Long-term, non-
669 anthropogenic groundwater storage changes simulated by three global-scale
670 hydrological models. Sci. Rep. 9:10746. DOI:10.1038/s41598-019-47219-z.
671 15. Li, B., Beaudoing, H. and Rodell, M. (2020). GLDAS Catchment Land
672 Surface Model L4 daily 0.25×0.25 degree GRACE-DA1, Version 2.2 [Data set].
673 NASA Goddard Earth Sciences Data and Information Services Center.
674 DOI:10.5067/TXBMLX370XX8.
675 16. Li, B., Rodell, M., Kumar, S. et al. (2019). Global GRACE data
676 assimilation for groundwater and drought monitoring: Advances and challenges.
677 Water Resour. Res. 55:7564–7586. DOI:10.1029/2018WR024618.
678 17. Copernicus Climate Change Service (2024). ERA5-Land post-
679 processed daily statistics from 1950 to present [Data set]. Copernicus Climate
680 Change Service (C3S) Climate Data Store (CDS). DOI:10.24381/cds.e9c9c792.
681 18. FAO (2019). SRTM DEM data on the Tibetan Plateau (2012) [Data set].
682 National Tibetan Plateau Data Center. DOI:10.11888/Geogra.tpdc.270486.
683 19. CGIAR-CSI (2004). Void-filled seamless SRTM data V1 [Data set].
684 International Centre for Tropical Agriculture (CIAT). Available at:
685 http://srtm.csi.cgiar.org.
686 20. Ran, Y., Li, X., Che, T. et al. (2022). Current state and past changes in
687 frozen ground at the Third Pole [Data set]. National Tibetan Plateau Data Center.
688 DOI:10.11888/Cryos.tpdc.272790.

21. Ran, Y., Li, X., Che, T. et al. (2022). Current state and past changes in frozen ground at the Third Pole: A research synthesis. Adv. Clim. Change Res. 13:632–641. DOI:10.1016/j.accre.2022.09.004.

22. Liu, S., Xu, N., Zhan, J. et al. (2023). Data set of socio-economic vulnerability parameters in agricultural and pastoral areas of Qinghai Tibet Plateau (2000-2020) [Data set]. National Tibetan Plateau Data Center. DOI:10.11888/HumanNat.tpdc.300897.

23. Zhang, G. (2019). Dataset of river basins map over the TP (2016) [Data set]. National Tibetan Plateau Data Center. DOI:10.11888/BaseGeography.tpe.249465.file.

24. Zhang, G.Q., Yao, T.D., Xie, H.J. et al. (2013). Increased mass over the Tibetan Plateau: From lakes or glaciers? Geophys. Res. Lett. 40:2125–2130. DOI:10.1002/grl.50462.

25. Department of Rural Socio-Economic Survey, National Bureau of Statistics of China (2001). China County Statistical Yearbook 2001 (China Statistics Press). [in Chinese]

26. Department of Rural Socio-Economic Survey, National Bureau of Statistics of China (2011). China County Statistical Yearbook 2011 (China Statistics Press). [in Chinese]

27. Department of Rural Socio-Economic Survey, National Bureau of Statistics of China (2021). China County Statistical Yearbook 2021 (China

710 Statistics Press). [in Chinese]

711 28. OpenStreetMap contributors (2026). OpenStreetMap [Data set].
712 OpenStreetMap Foundation. https://www.openstreetmap.org (accessed 7
713 November 2026).

714 29. Li, D. and Bai, Y.Y. (2024). Floods inventory in High Mountain Asia
715 (1950–2023) [Data set]. National Tibetan Plateau Data Center.
716 DOI:10.11888/HumanNat.tpdc.301724.

717 30. Bai, Y.Y., Li, D.F., Wangchuk, S. et al. (2025). Flood complexity and
718 rising exposure risk in High Mountain Asia under climate change. Sci. Bull.
719 70:1601–1604. DOI:10.1016/j.scib.2025.01.055.

720 31. Mayo, R., Zlydenko, O., Bootbool, M. et al. (2026). Groundsource: A
721 dataset of flood events from news [Data set]. Zenodo.
722 DOI:10.5281/zenodo.18647054.

723 32. Coles, S. (2001). An Introduction to Statistical Modeling of Extreme
724 Values (Springer). DOI:10.1007/978-1-4471-3675-0.

725 33. Hirsch, R.M., Slack, J.R. and Smith, R.A. (1982). Techniques of trend
726 analysis for monthly water quality data. Water Resour. Res. 18:107–121.
727 DOI:10.1029/WR018i001p00107.

728 34. Al-Shabeeb, A.R., Al-Adamat, R. and Mashagbah, A. (2016). AHP with
729 GIS for a preliminary site selection of wind turbines in the North West of Jordan.
730 Int. J. Geosci. 7:1208–1221. DOI:10.4236/ijg.2016.710090.

731 35. Diakoulaki, D., Mavrotas, G. and Papayannakis, L. (1995). Determining
732 objective weights in multiple criteria problems: The CRITIC method. Comput.
733 Oper. Res. 22:763–770. DOI:10.1016/0305-0548(94)00059-H.
734 36. Saaty, T.L. (1980). The Analytic Hierarchy Process: Planning, Priority
735 Setting, Resource Allocation (McGraw-Hill).
736 37. Xu, Z.S. and Da, Q.L. (2002). Study on method of combination
737 weighting. Chin. J. Manage. Sci. 10:84–87. [in Chinese]
738 38. Prokhorenkova, L., Gusev, G., Vorobev, A. et al. (2018). CatBoost:
739 Unbiased boosting with categorical features. In Advances in Neural Information
740 Processing Systems 31, S. Bengio, H. Wallach, H. Larochelle et al., eds.
741 (Curran Associates), pp. 6638–6648.
742 39. Lundberg, S.M. and Lee, S.-I. (2017). A unified approach to interpreting
743 model predictions. In Advances in Neural Information Processing Systems 30,
744 I. Guyon, U. von Luxburg, S. Bengio et al., eds. (Curran Associates), pp. 4765–
745 4774.
746 40. Lundberg, S.M., Erion, G., Chen, H. et al. (2020). From local
747 explanations to global understanding with explainable AI for trees. Nat. Mach.
748 Intell. 2:56–67. DOI:10.1038/s42256-019-0138-9.
749 41. Saltelli, A. and Annoni, P. (2010). How to avoid a perfunctory sensitivity
750 analysis. Environ. Model. Softw. 25:1508–1517.
751 DOI:10.1016/j.envsoft.2010.04.012.

752 42. Jenks, G.F. (1967). The data model concept in statistical mapping. Int.
753 Yearb. Cartogr. 7:186–190.
754 43. Chen, X.G., Yu, Z.B., Lin, H. et al. (2024). Hydrological responses to
755 permafrost degradation on Tibetan Plateau under changing climate. Water Sci.
756 Eng. 17:209–216. DOI:10.1016/j.wse.2024.04.002.
757 44. Qiu, X.P., Yang, X., Fang, Y. et al. (2018). Impacts of snow disaster on
758 rural livelihoods in southern Tibet-Qinghai Plateau. Int. J. Disaster Risk Reduct.
759 31:143–152. DOI:10.1016/j.ijdrr.2018.05.007.
760 45. Li, H., Zhao, X. and Wang, W. (2023). Evaluation and formation
761 mechanism of rural social vulnerability under natural hazard: A case study of
762 the eastern Qinghai-Tibetan Plateau, China. Habitat Int. 138:102871.
763 DOI:10.1016/j.habitatint.2023.102871.
764 46. He, X., Yan, J., Yang, E.L. et al. (2022). Climate change adaptation of
765 smallholders on the Tibetan Plateau under government interventions. J. Clean.
766 Prod. 381:135171. DOI:10.1016/j.jclepro.2022.135171.
767 47. Gao, X. and Sun, D. (2021). Transport accessibility and social demand:
768 A case study of the Tibetan Plateau. PLoS ONE 16:e0257028.
769 DOI:10.1371/journal.pone.0257028.
770 48. Moreira, L.L., de Brito, M.M. and Kobiyama, M. (2021). A systematic
771 review and future prospects of flood vulnerability indices. Nat. Hazards Earth
772 Syst. Sci. 21:1513–1530. DOI:10.5194/nhess-21-1513-2021.

773 49. Moreira, L.L., Vanelli, F.M., Schwamback, D. et al. (2023). Sensitivity
774 analysis of indicator weights for the construction of flood vulnerability indexes:
775 A participatory approach. Front. Water 5:970469.
776 DOI:10.3389/frwa.2023.970469.
777 50. de Brito, M.M., Almoradie, A. and Evers, M. (2019). Spatially-explicit
778 sensitivity and uncertainty analysis in a MCDA-based flood vulnerability model.
779 Int. J. Geogr. Inf. Sci. 33:1788–1806. DOI:10.1080/13658816.2019.1599125.
780 51. Song, J.Y. and Chung, E.S. (2016). Robustness, uncertainty and
781 sensitivity analyses of the TOPSIS method for quantitative climate change
782 vulnerability: A case study of flood damage. Water Resour. Manage. 30:4751–
783 4771. DOI:10.1007/s11269-016-1451-2.